Journal of the Korean Association of Geographic Information Studies, 21(4) 2018, pp. 26-49 ISSN 1226-9719(Print)
https://doi.org/10.11108/kagis.2018.21.4.026 ISSN 2287-6952(Online)

Radiation Flux Impact in High Density Residential Areas*
– A Case Study from Jungnang area, Seoul –

Chae-Yeon YI[1※]·Hyuk-Gi KWON[1]·Fredrik Lindberg[2]

고밀도 주거지역에서의 복사플럭스 영향 연구*
– 서울시 중랑구 지역을 대상으로 –

이채연[1※]·권혁기[1]·프레드릭 린드버그[2]

ABSTRACT

The purpose of this study was to verify the reliability of the solar radiation model and discuss its applicability to the urban area of Seoul for summer heat stress mitigation. We extended the study area closer to the city scale and enhanced the spatial resolution sufficiently to determine pedestrian-level urban radiance. The domain was a 4 km^2 residential area with high-rise building sites. Radiance modelling (SOLWEIG) was performed with LiDAR (Light Detection and Ranging)-based detailed geomorphological land cover shape. The radiance model was evaluated using surface energy balance (SEB) observations. The model showed the highest accuracy on a clear day in summer. When the mean radiation temperature (MRT) was simulated, the highest value was for a low-rise building area and road surface with a low shadow effect. On the other hand, for high-rise buildings and vegetated areas, the effect of shadows was large and showed a relatively low value of mean radiation temperature. The method proposed in this study exhibits high reliability for the management of heat stress in urban areas at pedestrian height. It is applicable for many urban micro-climate management functions related to natural and artificial urban settings; for example, when a new urban infrastructure is planned.

KEYWORDS : mean radiant temperature, sky view factor, SOLWEIG model, surface energy balance, urban radiant flux.

2018년 11월 05일 접수 Received on November 5, 2018 / 2018년 11월 19일 수정 Revised on November 19, 2018 / 2018년 11월 21일 심사완료 Accepted on November 21, 2018

* 이 연구는 기상청 <자연재해대응 영향예보 생산기술 개발>(KMI2018-01410)의 지원으로 수행되었습니다.

1 한국외국어대학교 대기환경연구센터 Research Center for Atmospheric Environment, Hankuk University of Foreign Studies, Yongin, Korea

2 괴텐버그대학교 지구과학과 Dept. of Earth Sciences, University of Gothenburg, Gothenburg, Sweden

※ Corresponding Author E-mail : prpr.chaeyeon@gmail.com

요 약

본 연구는 도시지역을 대상으로 태양복사모델링을 수행하고 검증하여, 도시 내 열스트레스 완화에 대한 적용 가능성을 논의하였다. 이를 위해 연구지역은 항공 LiDAR 자료를 기반으로 실제 건물과 식생의 형태와 높이가 구현되었고, 보행자높이에서의 단파 및 장파복사 플럭스가 모의될 수 있도록 해상도를 향상시켰다. 고층 및 저층 건물이 고밀도로 존재하는 주거지역 4㎢에서 SOLWEIG 모델을 이용하여 복사플럭스를 모의하고, 지표에너지수지시스템의 Net radiometer를 이용한 복사플럭스 관측자료로 검증하였다. 그 결과 여름철 맑은 날 가장 높은 정확도를 나타냈고, 같은 날에 대한 평균복사온도를 모의한 결과, 그림자영향이 적은 저층 건물지역과 도로표면에서 가장 높은 수치를 나타냈으며, 고층 건물지역과 식생지역에서는 그림자의 영향으로 상대적으로 낮은 수치를 나타냈다. 본 연구에서 제안된 방법은 보행자높이에서 도시 내 열스트레스 지역 관리를 위한 높은 신뢰도를 보여주었다. 더욱 확장되고 있는 도시재생 및 재개발에 있어서, 새로운 주거환경을 도입하기 위해 도시 기반시설을 계획할 때 자연 및 인공 도시환경 설정과 관련된 많은 기능이 적용될 수 있다.

주요어 : 평균복사온도, 하늘시계지수, SOLWEIG모델, 지표면 에너지 밸런스, 도시복사 플럭스

Introduction

If current population growth and urbanisation continue, the Seoul metropolitan urban area will triple from approximately 400,000 km^2 in 2010 to 1.2 million km^2 in 2030; 90% of the world's population (approximately 8 billion people) will live in cities by 2025. The urbanised area in Korea has increased by approximately 95%, from 2,133 km^2 (2.1% of the national land area) in the 1980s, to 4,154 km^2 (4.1% of the national land area) in the 2000s (Ministry of Environment, 2011). As a result of this urban growth, the density of artificial cover, such as asphalt and concrete, is expected to increase. This in turn is expected to greatly enhance the heat reserves that can be physically stored in cities, exacerbating the urban heat island and related extreme weather. Future effects of global climate change on an urban micro-climate scale may include various pedestrian-level extreme weather phenomena (e.g., heat waves).

The land cover that constitutes the urban surface is an important factor that determines the local air temperature and thermal comfort of residents. Urban buildings and forests are linked to physical processes such as evapotranspiration, filtration, permeation, absorption, and reflection of solar radiation (Akbari, 2001). As the proportion of high heat capacity asphalt and concrete increases, the city transitions away from a comfortable climate zone. Eventually, it develops a unique micro-structure that is hotter in summer and more regionally variable in winter. Given its effects on general urban activities such as energy demand and supply, the radiation balance of the land surface is key to establishing a sustainable and safe urban environment

during urban land use planning. Therefore, the spatial management of surface cover is related to the management of urban micro-climate (An *et al.*, 2016b). In Korea, studies on the thermal environment have been conducted (Kim *et al.,* 2014) to explain changes in the intensity of urban heat islands (UHI) due to urban solar radiation and the resulting changes in heat stress and disease. In addition, climate analysis tools that reflect the physical complexity of cities and relate to thermal comfort are being improved (Jaenicke *et al.,* 2016; Yi *et al.,* 2016). The thermal environment distribution and thermal island intensity analysis model explain the differences in the degrees of inhomogeneous solar radiation and surface radiation caused by urban geometry. The urban thermal environment is also heterogeneously distributed owing to the complexity of the city, where differences in structure and form vary widely. The sky view factor (SVF) is a major spatial factor that explains this structural complexity (An *et al.,* 2014, Yi *et al.,* 2017). Air temperature, mean radiant temperature, air velocity, and humidity are well known physical factors that affect body temperature control and thermal comfort. Several variables also affect various ecosystem cycles and life activities (An *et al.,* 2014).

The mean radiant temperature (T_{mrt}) is one of the most important meteorological parameters associated with human life, representing the energy balance and thermal comfort of the human body (ASHRAE, 2001). It is the mean temperature of the surrounding surface that exchanges heat with the body via radiation. The mean radiant temperature is the sum of shortwave and longwave radiation fluxes (direct and diffuse), which can be evaluated quantitatively and specifically to indicate human heat stress (Lindberg *et al.,* 2008). Spatial information that directly reflects the actual physical environment in which citizens live is necessary to understand thermal vulnerability. The SOLWEIG (Solar and Long-Wave Environmental Irradiance Geometry) model simulates solar shortwave and longwave radiation from spatial structures and is used in bio-climate studies (e.g. An *et al.,* 2016a; Jaenicke *et al.,* 2016; Konarska *et al.,* 2013; Lindberg *et al.,* 2008; Lindberg and Grimmond 2011). Kim *et al.* (2014), in conjunction with SOLWEIG and KMM, developed a model to estimate the number of excess deaths during heat waves by calculating the perceived temperature (PT) from hourly T_{mrt} for both old and new cities. However, we still do not use T_{mrt} as a scientific marker for urban micro-climate management, mainly owing to a lack of city scale and pedestrian-level spatial data and sufficient validation of its reliability.

The purpose of this study was to expand the research area close to the urban scale and to improve radiation modelling research by ensuring sufficient spatial resolution to investigate urban radiation at the pedestrian level. Net radiometer observations were used to evaluate the

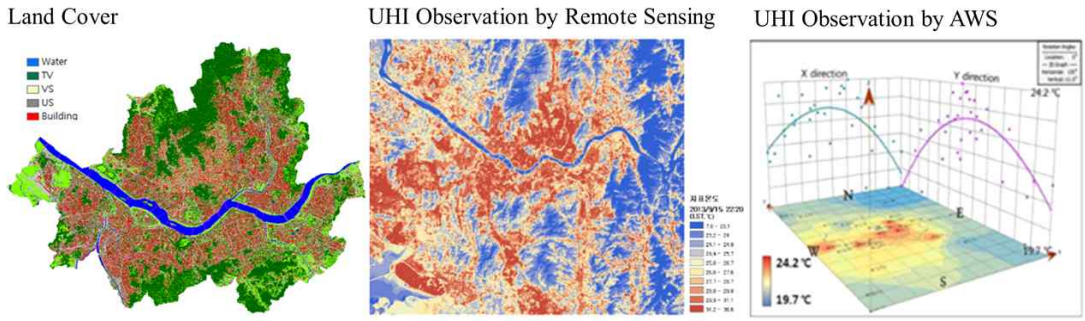

FIGURE 1. Urban settings (land cover) and observed urban heat islands (UHI) in Seoul (Source: An *et al.*, 2016b)

accuracy of the daily solar radiation model for weather cases and to improve the reliability of the mean radiant temperature results. In addition, we considered the feasibility of application to areas with high heat stress by type of buildings for clear summer days, on which heat-waves frequently occur in Seoul.

Methods and data

1. Urban settings and urban heat island in Seoul metropolitan area

In Seoul, forest canopy covers approximately 40% of the administrative area. However, most of the forest cover is located in mountainous not residential areas. Seamless urban growth has accelerated the decline of residential area forest canopy cover in the Seoul metropolitan area (SMA), similar to other northern mid-latitude cities. Vulnerability to climate change in urban areas is mainly due to the urban sprawl process that causes a decrease in forests with an increase in asphalt and concrete infrastructure (Fig. 1). Hence, a scientifically informed urban setting strategy is required to manage summer heat island mitigation in SMA. The strategy should be both reliable and easy to understand as a healthy urban planning tool that can offset the impacts of urban climate change such as summer heat stroke.

2. SOLWEIG model

The SOLWEIG model was developed by the Urban Climate Group, University of Gothenburg, Sweden (Lindberg *et al.*, 2008). Version 1.0 was released in 2009, and the 2013a version was used in this study. The SOLWEIG model interface was built using the Matlab Compiler Runtime (MCR). Using the T_{mrt} calculated in the model, it is possible to numerically simulate spatial and temporal changes at the building scale and at ground level. The SOLWEIG model uses the sky view factor for vegetation, buildings, and ground; the shadow effect; temperature; humidity; and solar radiation data to calculate the three-dimensional shortwave and longwave radiation and

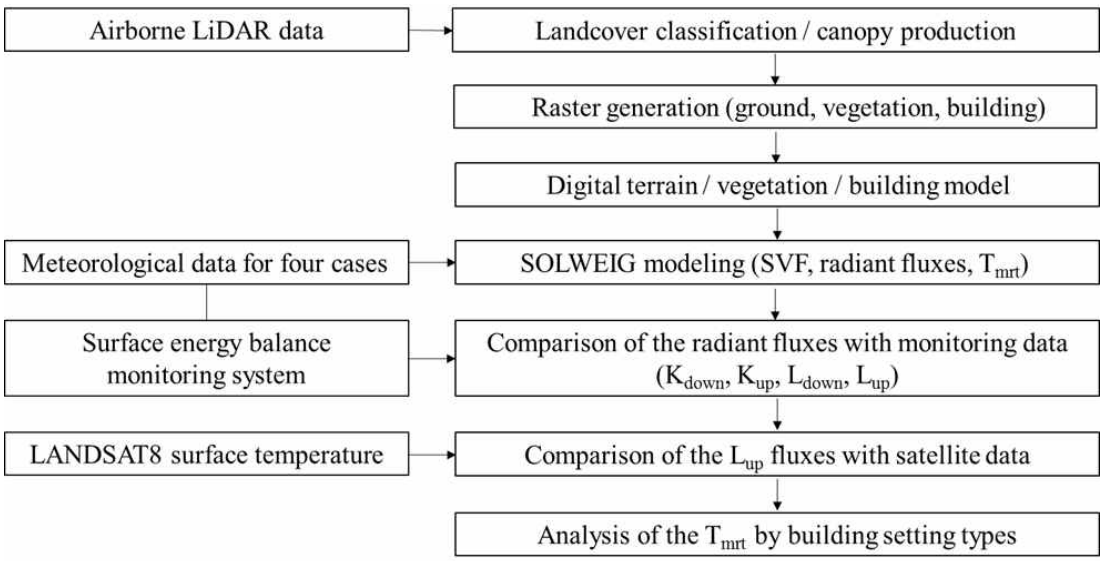

FIGURE 2. Flowchart showing the procedure followed in this study.

the T_{mrt} (Fig. 2). For the calculation of T_{mrt}, the mean radiant flux density factors (S_{str}) and the individual absorption factors of three-dimensional longwave and shortwave radiation are required (VDI, 1994).

$$S_{str} = \xi_k \cdot \sum_{i=1}^{6} K_i \cdot F_i + \varepsilon_p \cdot \sum_{i=1}^{6} L_i \cdot F_i \quad (1)$$

In Eq. 1, K_i and L_i are the longwave and shortwave radiation fluxes in each of six directions (East, West, South, North, Up, Down) and F_i is the radiation flux of each angular factor, which is 0.22 for radiation in the cardinal directions and 0.06 for up and down radiation directions. The ξ_{k_i} is the shortwave absorption coefficient (0.7) and ε_p can be the absorption rate of the human body (0.97). If S_{str} is obtained, T_{mrt} is calculated by the Stefan-Boltzmann law:

$$T_{mrt} = \sqrt[4]{(S_{str}/(\epsilon_p \cdot \sigma))} + 273.15 \quad (2)$$

where σ is the Stefan-Boltzmann constant (5.67×10^{-8} Wm^{-2} K^{-4}). The shortwave radiation flux uses direct radiation, diffuse radiation, and global radiation as input data. The shortwave radiation ($K_{\downarrow ij}$) flowing into a particular location in the city is calculated via Eq. 3:

$$K_{\downarrow ij} = K_{dir} \times Sh_{ij} \times \sin\eta + K_{diff} \times \Psi_{ij} + G \times \alpha \times (1 - \Psi_{ij}) \times \sin\eta \quad (3)$$

$$\Psi_{ij} = \left(\frac{1 - \cos\theta)}{2} \right) = (1 - (\Psi_{wall1} + \Psi_{wall2})) \quad (3a)$$

where K_{dir}, K_{diff}, and G are direct radiation, diffuse radiation, and global

radiation, respectively; η is a Boolean value to determine the yes (0) or no (1) condition of the shadow at the matrix i × j location; and Ψ_{ij} is the solar altitude (angle between the horizon and the sun). In Eq. 3a applies a raster-based calculation method developed by Ratti and Richens (1999) with a SVF at the matrix i × j location and with α as the average albedo of all surrounding surfaces (0.15). Eq. (3) simplifies the direct radiation and diffuse radiation flux and the reflected radiation due to the surface. The amount of direct radiation that reaches the surface and escapes by reflection from the surface is estimated by Eq. 4:

$$K_{\uparrow ij} = K_{\downarrow ij} \times \alpha \tag{4}$$

The longwave radiation ($L_{\downarrow ij}$) incident at the matrix i × j location is calculated from the input air temperature (T_a) and relative humidity (RH) information:

$$L_{\downarrow ij} = \Psi_{ij}\epsilon_{sky}\sigma T_a^4 + (1-\Psi_{ij})\epsilon_w \sigma T_s^4 + (1-\Psi_{ij})(1-\epsilon_w)\epsilon_{sky}\sigma T_a^4 \tag{5}$$

where ε_{sky} and ε_w are the longwave radiation from the sky and walls, respectively; T_s is the longwave radiation from the sky with the average surface temperature (K) of the building, wall, and ground, longwave radiation from the wall, and longwave radiation from the reflected sky.

If there are clouds in the sky, the total effective emission longwave radiation from the sky increases, so that the longwave radiation incident is transformed as shown in Eq. 6:

$$L_{\downarrow ij} = L_{\downarrow ij_c} \cdot (1-c) + c \cdot \sigma T_a^4 \tag{6}$$

where c is the fractional cloud cover ($0 \le c \le 1$).

The detailed method for calculating T_{mrt} is described in Lindberg *et al.* (2008) and Lindberg and Grimmond (2011). Recently, a physical scheme with land cover has been used and integrated into the Urban Multi-scale Environmental Predictor (UMEP) to improve this environment prediction tool (Lindberg *et al.,* 2016, 2018).

3. SMA surface energy balance monitoring system

The urban surface energy balance (SEB) monitoring system installed by the Weather Information Service Engine (WISE) and operated by the Research Center for Atmospheric Environment (RCAE) and Korea Meteorological Administration (KMA) is installed at 14 sites in the SMA (Park *et al.,* 2017). In this study, we used net radiometer data from the SEB system in the Jungnang area, a representative compact low-rise residential area of Seoul. As of 4 December 2013, the building height was 14 m and the observation tower height was 18.5 m. The observed altitude of the meteorological data required for modelling with SOLWEIG is 16 m, the composite sensors for temperature, humidity, and wind speed are at 4 m, 10 m, and 18 m, respectively, and the

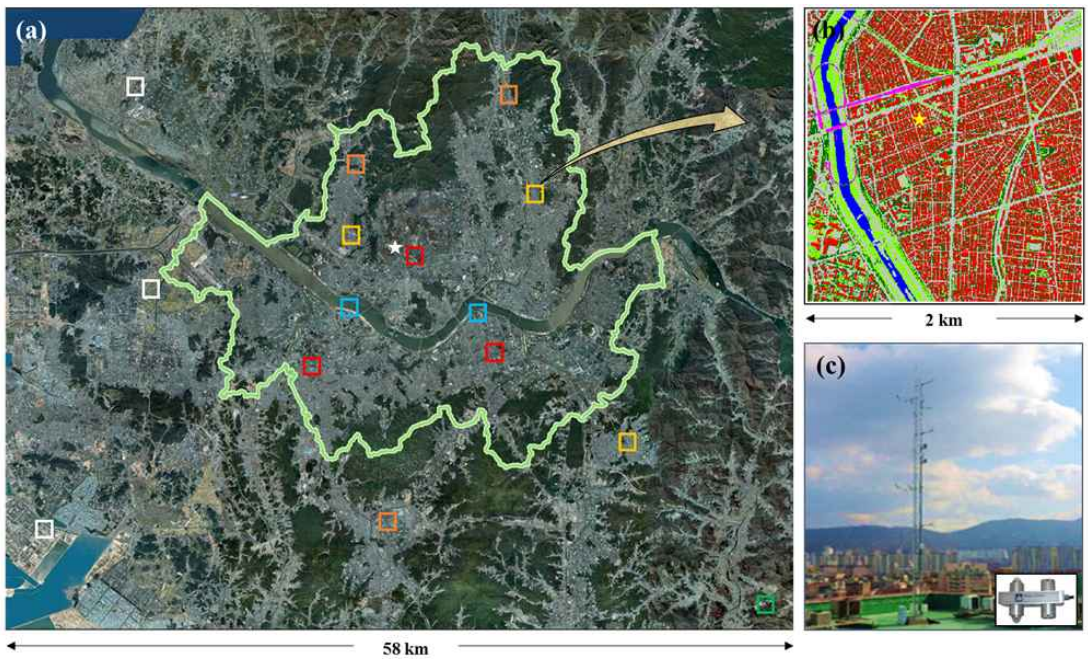

FIGURE 3. Surface energy balance (SEB) system in the Seoul Metropolitan Area (SMA) and surrounding environment. (a) White is the reference area, orange is the high-rise residential area, yellow is the low-rise residential area, red is the commercial area, and blue is water. The white star denotes the weather station. (b) Close-up of land cover in a high-rise residential area (4 km^2) and observation equipment installation point (denoted by the yellow star). (c) Image of the surface energy balance (SEB) monitoring system tower.

radiation and radiant flux is at 16 m (Fig. 3). The land cover around the tower within a 600 m radius is 48% residential area, 6% apartment complexes, and 1% school buildings (Kwon *et al.,* 2014). The local climate zone (LCZ) classification places the Jungnang SEB system in zone 2E (compact low-rise; Stewart and Oke, 2012).

4. High-resolution model inputs for realistic urban settings

High-resolution surface information and meteorological data are required for SOLWEIG operation. The input surface information data was converted into raster format using the classification results from 3D point cloud data obtained from airborne LiDAR data. The airborne LiDAR data were acquired using a Leica Airborne Laser Scanner 60 at an altitude of approximately 700 m a.g.l. (above ground level) on 6 September, 2008 (12 bit, 100 kHz, l 50°) with a point data density of 2.5 to 10 point m^{-2} (An *et al.,* 2016a, Yi *et al.,* 2012). The surface input data for SOLWEIG are DSM (digital surface model) for building height and area information, Vegetation_DEM for

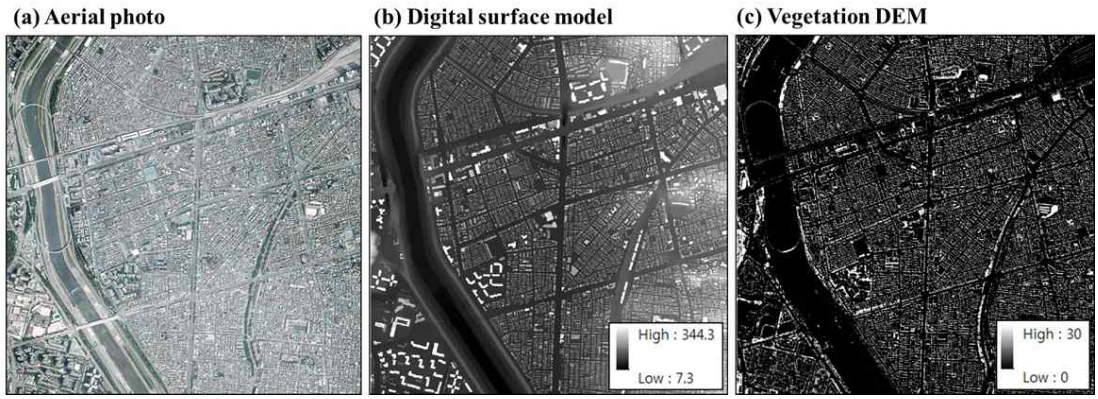

FIGURE 4. Surface input data (2 m grid) for SOLWEIG.

vegetation height and area information, and Trunk_DEM for tree circumference and height information (Fig. 4). Trunk_DEM is calculated as 1/4 of the tree height, but the maximum value is 30 m considering the resolution of the model input data (user manual for SOLWEIG version 2013a, 2013). Table 1 shows the input parameters for calculating the T_{mrt}, shadow pattern, and SVF.

5. Weather data for SOLWEIG modelling

A case study for evaluating radiant fluxes covered four days: clear/sunny and cloudy days in summer and winter. To determine appropriate clear/sunny and cloudy days using the cloud data at Seoul weather station (SWS) for 2014, we compared the air temperature data from SWS with air temperature data from the SEB system in the Jungnang area (Fig. 3). The SWS has an hourly dose of incoming shortwave radiation data, and cloud amount data. The solar radiation and meteorological data of the SWS were input into the model, and the results were estimated with the radiant flux data of Jungnang SEB. The statistical correlation coefficient (R^2) calculated from the air temperature data at both sites was 0.85. Precipitation days were excluded because of the high error in the radiation observation sensor (Lindberg *et al.,* 2008). According to the cloud extent, a clear day was selected when the daily average cloud cover was <

TABLE 1. Input parameters for SOLWEIG simulation.

Category	Input for simulations
Geographical location (latitude/ longitude/ altitude/ UTC)	127° / 37.6° / 87 m/ +9
Personal parameters (absorption [shortwave]/ absorption [longwave]/ posture)	0.7/ 0.95/ standing
Urban parameters (albedo [walls]/ albedo [ground]/ emissivity [walls]/ emissivity [ground]/ transmissivity [vegetation])	0.2/ 0.2/ 0.9/ 0.95/ 0.02

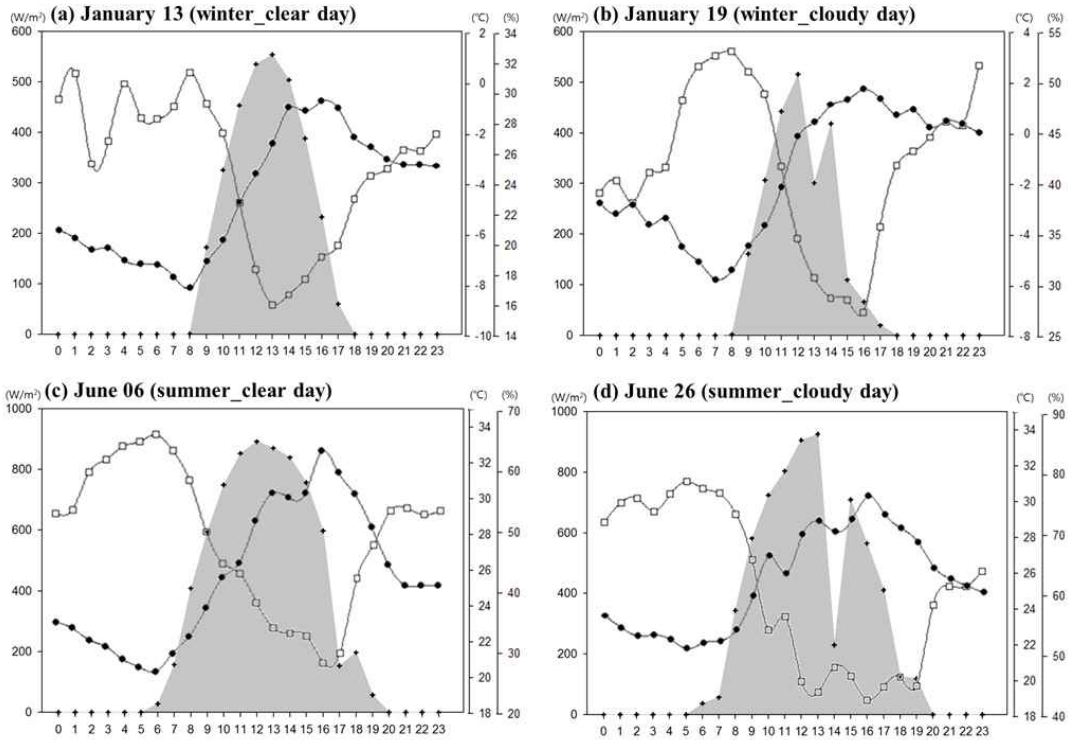

FIGURE 5. Weather data for the four case studies (black circles are temperature (℃), white circles are relative humidity (%), and shading is solar radiation (Wm^{-2}).

20% and a cloudy day was selected when the average cloud cover was > 50% at Seoul weather station. For winter, 13 January and 19 January were selected as clear and cloudy days, respectively; for summer, 6 June and 26 June were selected as clear and cloudy days, respectively (Table 2). The daily solar radiation graph shows clear differences between sunny and

TABLE 2. Cloud and solar radiation conditions corresponding to case study days using Seoul weather station data.

Season	Weather	Date	R^2	Cloud cover (10%)	Incoming shortwave radiation max. (Wm^{-2})	Incoming shortwave radiation mean (Wm^{-2})
Winter	Clear day	2014 01-13	0.98	0.0	553.85	134.33
	Cloudy day	2014 01-19	0.89	5.0	515.49	97.49
Summer	Clear day	2014 06-06	0.97	1.4	891.08	297.86
	Cloudy day	2014 06-26	0.85	5.9	926.03	272.28

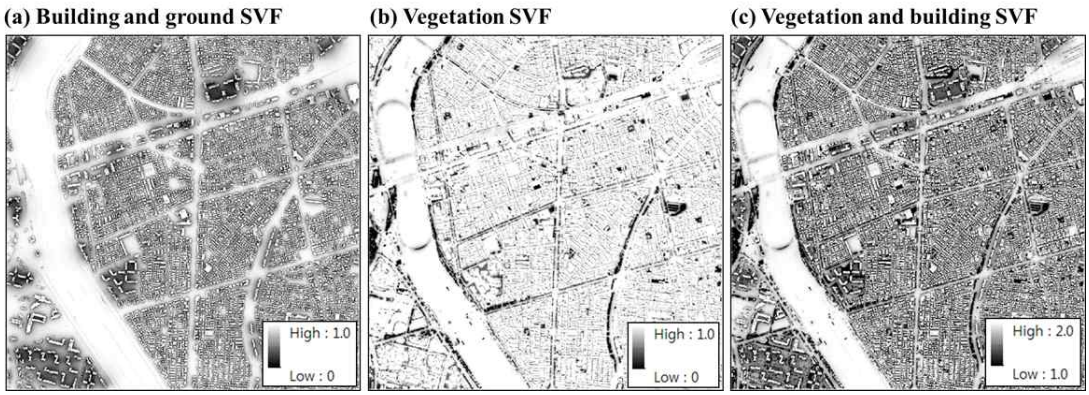

FIGURE 6. Sky view factor (SVF) for (a) buildings, (b) buildings and vegetation, and (c) vegetation in the Jungnang area.

cloudy days (Fig. 5).

6. Influence diameter (SEB measurement vs. SOLWEIG)

The SEB system net radiometer sensor was installed at a relatively high position to obtain representative weather data for the surrounding area. A previous study (Wang *et al.,* 2014) was used to calculate the precise influence radius based on the 18.5 m tower, 14 m building, and net radiometer used for evaluation (Eq. 7). The influence radius was calculated using the height of the sensor, including building height, and half of the field of view. Here, the half field of view was 75 a:

$$f = 2H \cdot \tan(HFOV^{*}) \quad (7)$$

where f is the influence diameter, H is the sensor height (including building height), and $HFOV^{*}$ is half of the field of view. Using Eq. (7), the influence radius of the sensor was calculated as 120 m and the model result shows the average value of all grids within this influence radius. An evaluation was performed by comparing the results with the observed values.

Results and discussion

1. Sky view factor and shadow trend analysis

SVF varies depending on the building, terrain, and vegetation height (Fig. 6). Higher SVF values result in higher daytime solar radiation without affecting the surrounding structures; the emission of surface radiation at night is also affected. SVF due to buildings and terrain varies greatly depending on the height and layout of the building (Fig. 6a). The SVF was low in the vicinity of the apartment complex (approximately 0.4) compared with near a low-rise multi-family housing complex (approximately 0.7). For vegetation (Fig. 6c), low SVF appeared at the point where the roadside

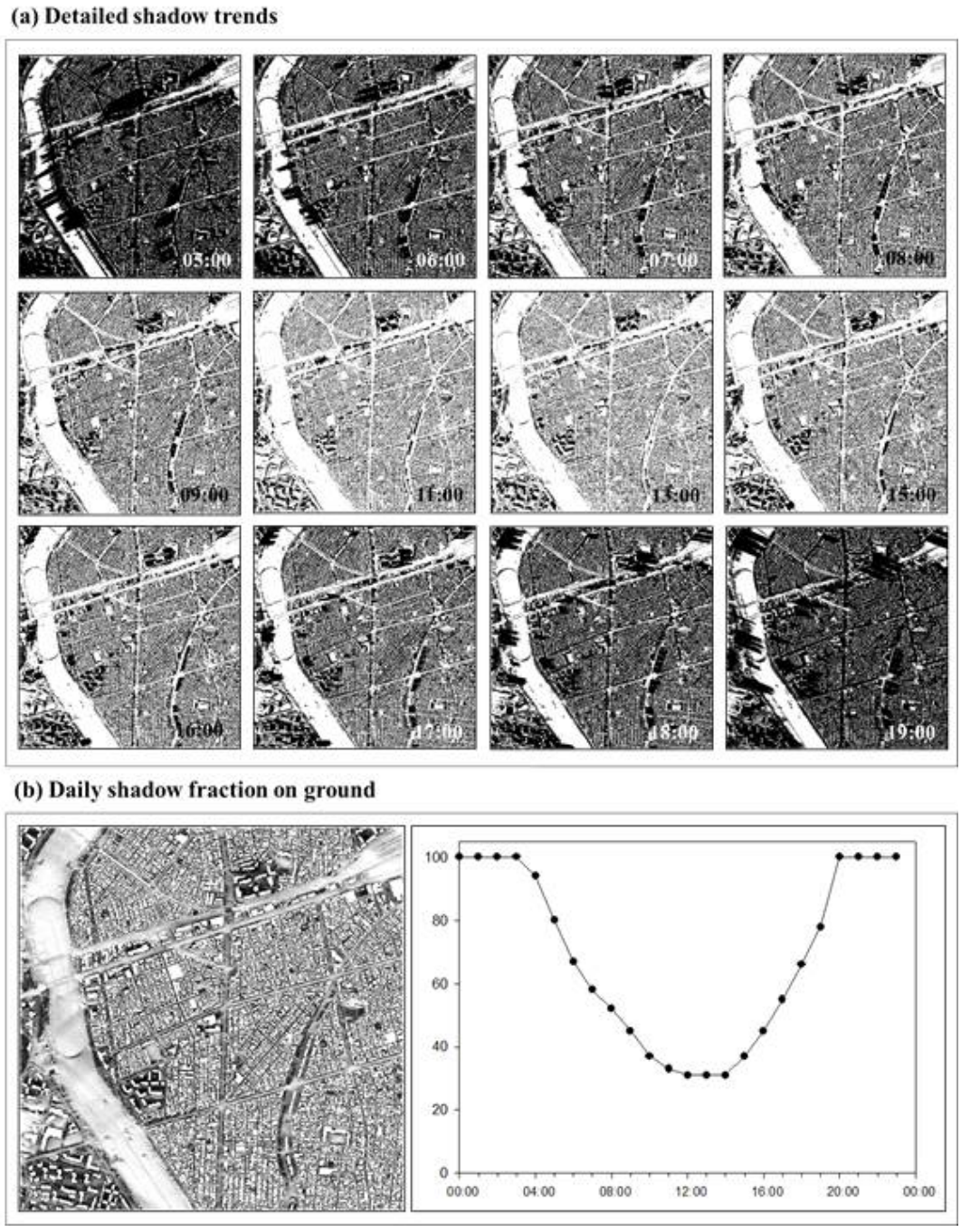

FIGURE 7. (a) Detailed shadow trends at one-hour intervals for June, 06, 2014 for the Jungnang area. (b) Daily average shadow distribution on the ground excluding buildings (left) and plot of shadow fraction (%) at ground level for each time step (right).

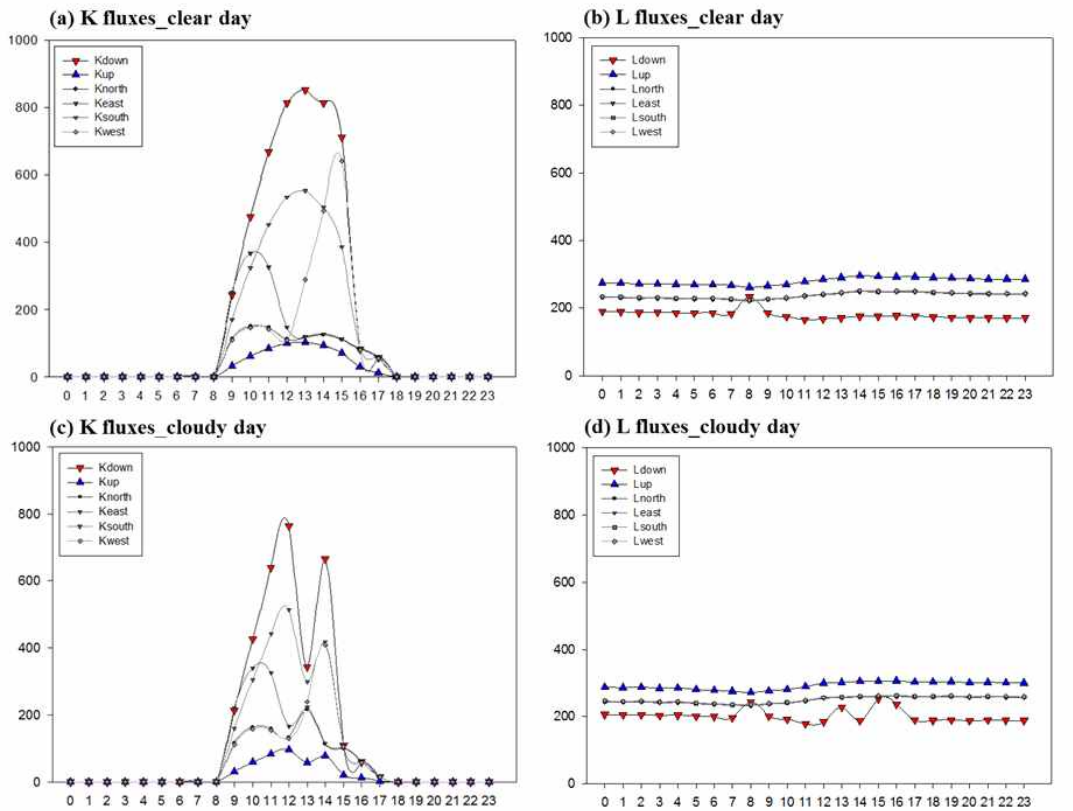

FIGURE 8. Comparison of shortwave radiation (K fluxes) and longwave radiation (L fluxes) on clear and cloudy days in winter.

(approximately 0.1) meets vegetation and depended on vegetation height. In the SOLWEIG model, we calculated SVF in the north, south, east, and west directions, and the average SVF using topography, building height, and vegetation height data. In addition, we analysed the shadow trends at 30 min intervals from sunrise to sunset using the latitude and longitude coordinates of the domain area and date (Fig. 7). The shadow patterns are also different depending on the position and height of the structure. As the sun rises from the east, shadows form west of the structure and long shadows appear around apartment complexes for tall buildings. The decrease in solar radiation due to the shadow effect during the day also affects the T_{mrt}. A detailed shadow pattern analysis every 30 minutes can be used to analyse the difference in daylight hours at each grid point and the influence of surrounding structures.

2. Radiation flux analysis from SOLWEIG

For the four case study days (cloudy and clear days in summer and winter)

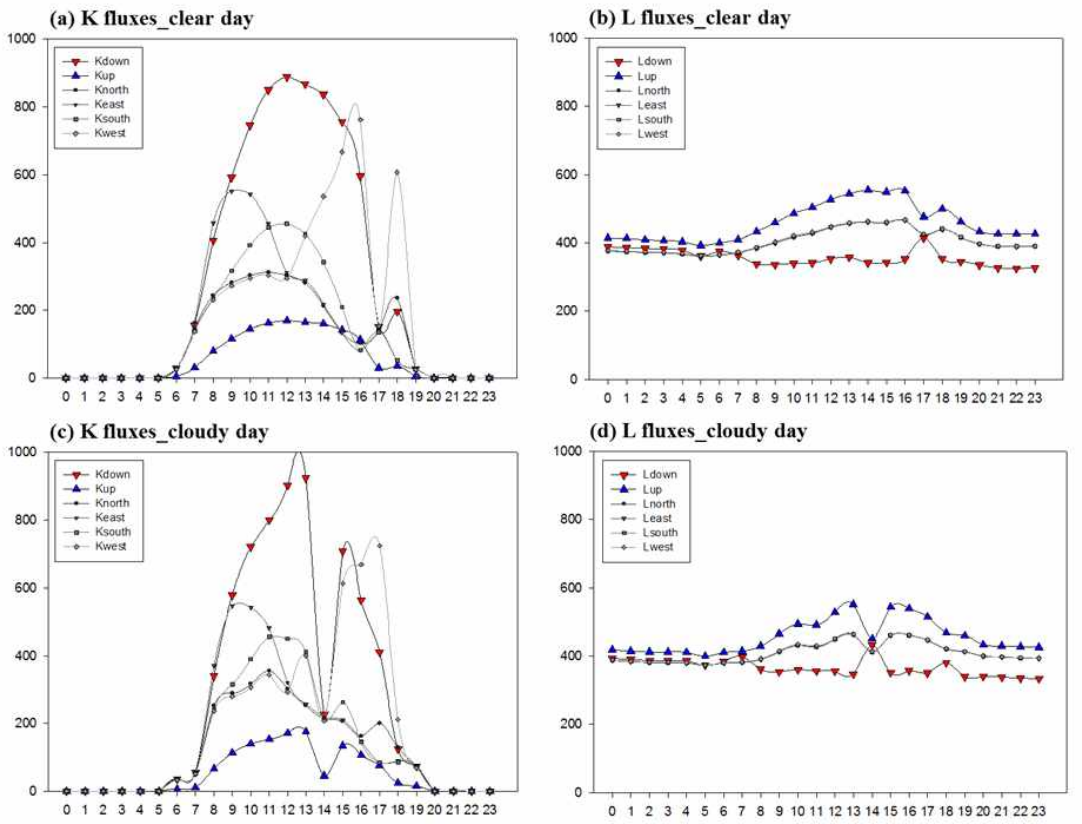

FIGURE 9. Comparison of shortwave radiation (K fluxes) and longwave radiation (L fluxes) on clear and cloudy days in summer.

meteorological data were input to simulate the radiation flux. The radiation flux was divided into shortwave (K fluxes) and longwave (L fluxes), and into six directions: upward, downward, east, west, south, and north. The K fluxes represented the amount of shortwave radiation emitted from the sun, expressed in watts per unit area. The fluxes reaching the city surface were called K_{down} fluxes, and K_{up} when they were reflected by aerosols and emitted again. L fluxes include longwave radiation from the surface; those that move upward were termed L_{up} fluxes and those that move downward due to surrounding structures or atmospheric reflection were termed L_{down} fluxes.

In winter, K fluxes were affected from 08:00 to 17:00, and K_{down} had a smaller solar time than in summer with figures below 600 Wm^{-2} (Fig. 8. a and c). The K fluxes along the east (K_{east}), west (K_{west}), north (K_{north}), and south (K_{south}) directions varied with the movement of the sun. On cloudy days, K_{down} was affected by decreased solar irradiation. The L fluxes emitted from the surface of the Earth are quite

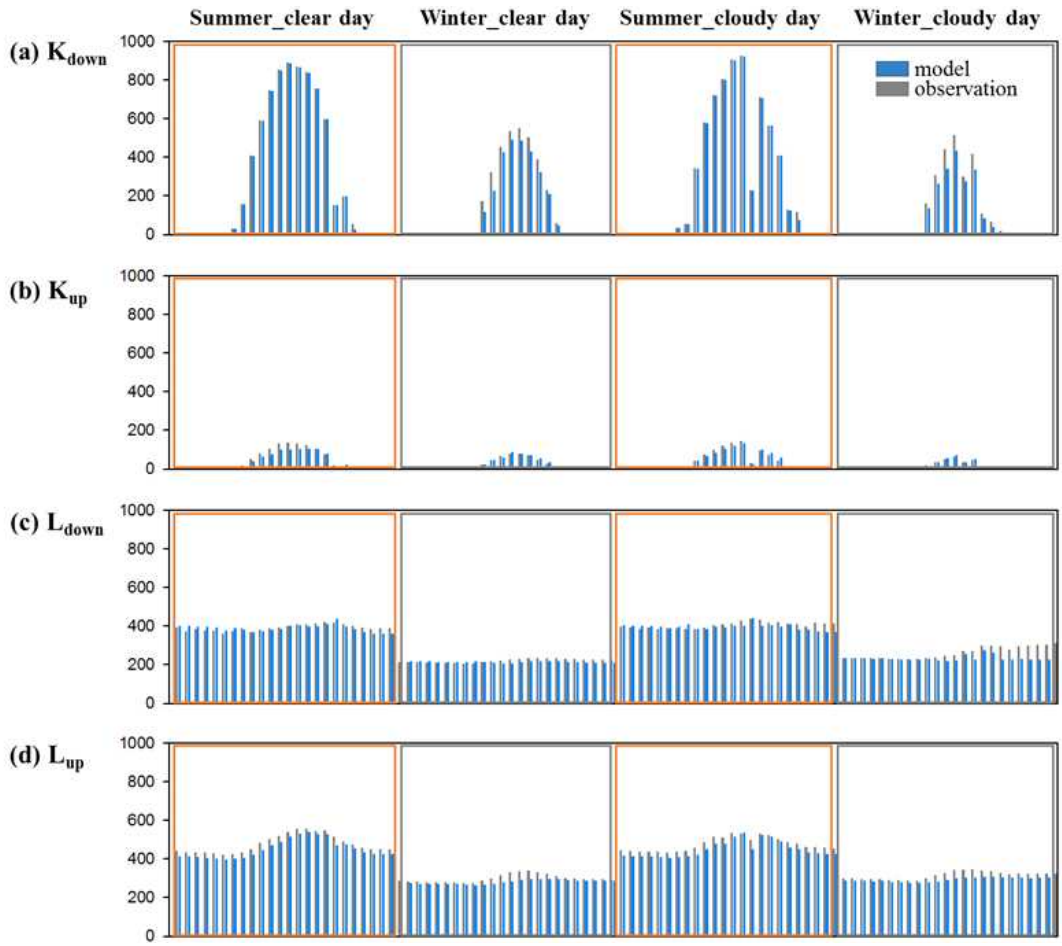

FIGURE 10. Observed and simulated radiation flux for four case studies. Orange and grey boxes indicate summer and winter, respectively. Sky blue bars show the model values and grey bars show the observation values. The x-axis is time (LST) and the y-axis is the radiation flux.

reliable. In summer, K fluxes were affected from 06:00 to 19:00, and the maximum value of K_{down} was approximately 900 Wm^{-2} (Fig. 9. a and c). The K_{east}, K_{west}, K_{north}, and K_{south} varied with time according to the movement of the sun. The K_{up} radiated in the atmosphere is approximately 200 Wm^{-2}, and K_{down} and K_{up} changed with decreased solar irradiation due to cloud. The L fluxes radiated from the surface appeared to increase slightly during the daytime.

3. SOLWEIG evaluation

The simulated radiant fluxes were evaluated using net radiometer data for all four weather types based on the methods described in Lindberg *et al.* (2008). As the net radiometer equipment does not observe the east, west, north, and south fluxes, only

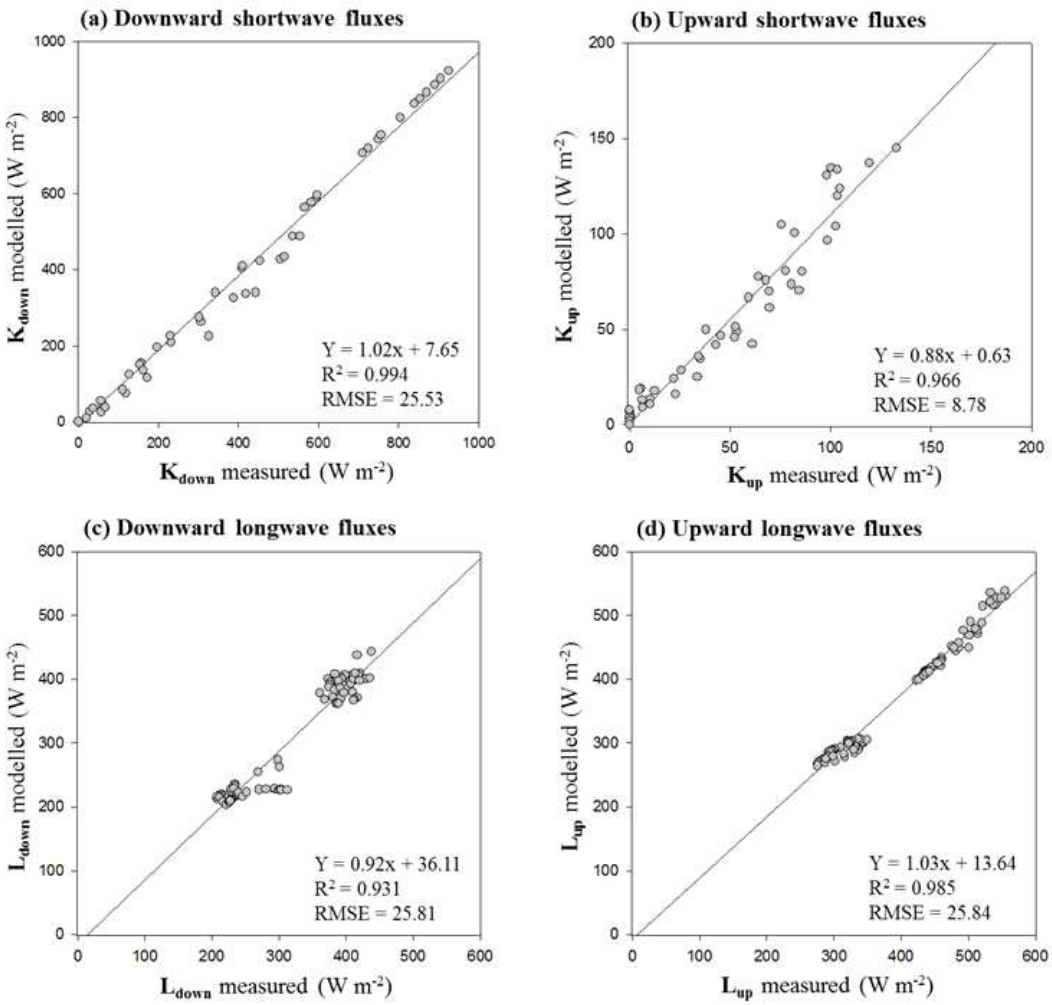

FIGURE 11. Correlation of measured radiant flux values with those simulated by the SOLWEIG model.

upward and downward fluxes data were used for verification.

For shortwave radiation (K fluxes), the downward (K_{down}) fluxes of the model and observations were similar in summer. In winter, the observed values were approximately 80 Wm^{-2} higher for both clear and cloudy days. The upward shortwave (K_{up} fluxes) fluxes showed similar patterns for the four case study days, with no significant differences between the model and the observations.

The L_{down} fluxes in winter were different from the observations on cloudy days (Fig. 10c), with L_{down} fluxes depending on longwave radiation coming from the average surface temperature of

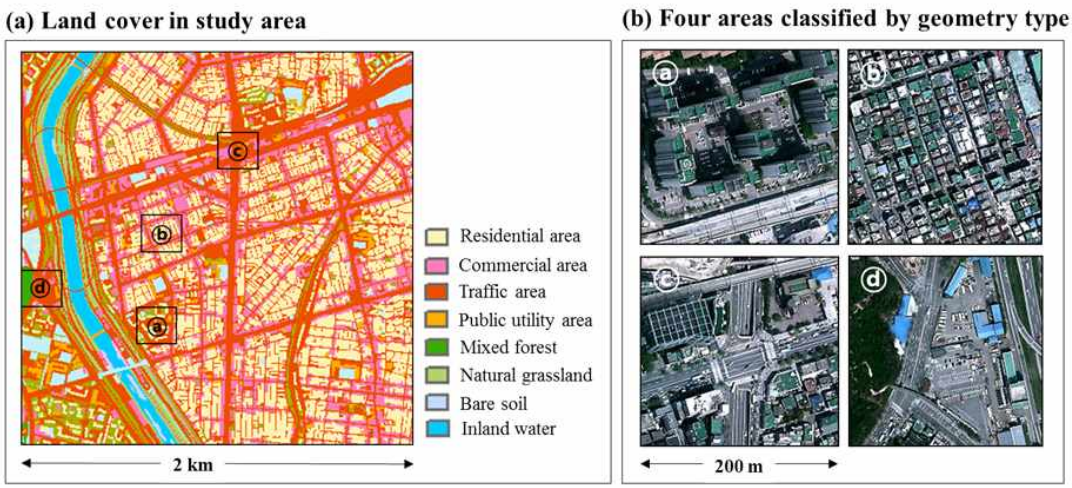

FIGURE 12. (a) Land cover data in the Jungnang area and (b) four urban settings classified by building type: 'a' open high–rise, 'b' compact low–rise, 'c' road, and 'd' vegetated area.

the walls and ground. The total effective radiated longwave radiation differs by quantity (An *et al.,* 2016a). The observation equipment was open–form (16 m above the roof of the building), and so it appeared to increase with the amount of local cloud. Furthermore, it is possible that there is a geographical difference between the site where the meteorological (temperature, humidity, radiation) input data for the model was collected and the simulation area. Owing to these results, it was necessary to input the local difference into the meteorological input, apply the spatial distribution to more than the representative data of one point, and make corrections to reflect the local characteristics.

In the case of the L_{up} fluxes (Fig. 10d), the model and observations differed by approximately 10 Wm^{-2} in summer, and the trend over time is similarly simulated. In winter, the difference between the model and the observation is 40 Wm^{-2}, but the observed data trends for daytime maximum L_{up} fluxes were not similarly simulated. Variables that could affect the observed L_{up} fluxes are the surface temperatures of surrounding objects and the presence of shadows, which may have affected local anthropogenic heat emission factors, and the difference between the observation and model altitudes.

A scattering analysis with the same number of samples (n = 96) provided a measure of correlation using the R^2 value (Fig. 11, Lindberg *et al.,* 2008). The values obtained for the fluxes indicate that they were significantly correlated, with R^2 values of 0.99, 0.96, 0.93, and 0.98 for K_{down}, K_{up}, L_{down}, and L_{up}, respectively. These are similar correlations to those found in the

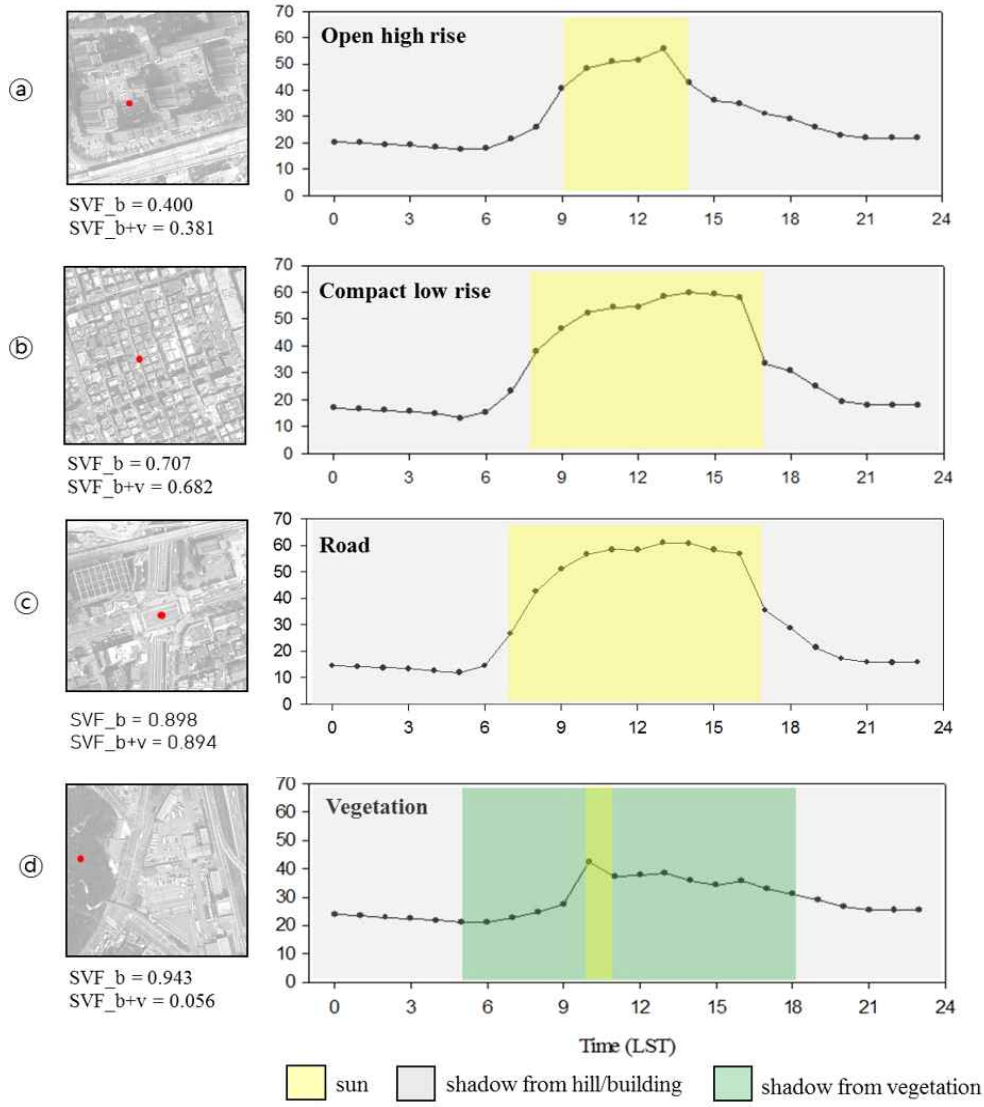

FIGURE 13. T_{mrt} at points of interest (red dots) in the four local urban building settings. T_{mrt} values are calculated at the pedestrian level according to time (6, June 2014).

literature (0.97, 0.97, 0.73, 0.94), indicating that SOLWEIG accurately simulates observed fluxes according to the surrounding buildings and vegetation and regardless of the weather. The Root Mean Square Error (RMSE) metric also indicated that the simulation performs well; RMSE values are 25.53, 8.78, 25.81, and 25.84 Wm^{-2} for K_{down}, K_{up}, L_{down}, and L_{up}, respectively. In summary, the model fairly accurately simulates the changes and values of radiant fluxes in residential areas and indicates the feasibility of obtaining a

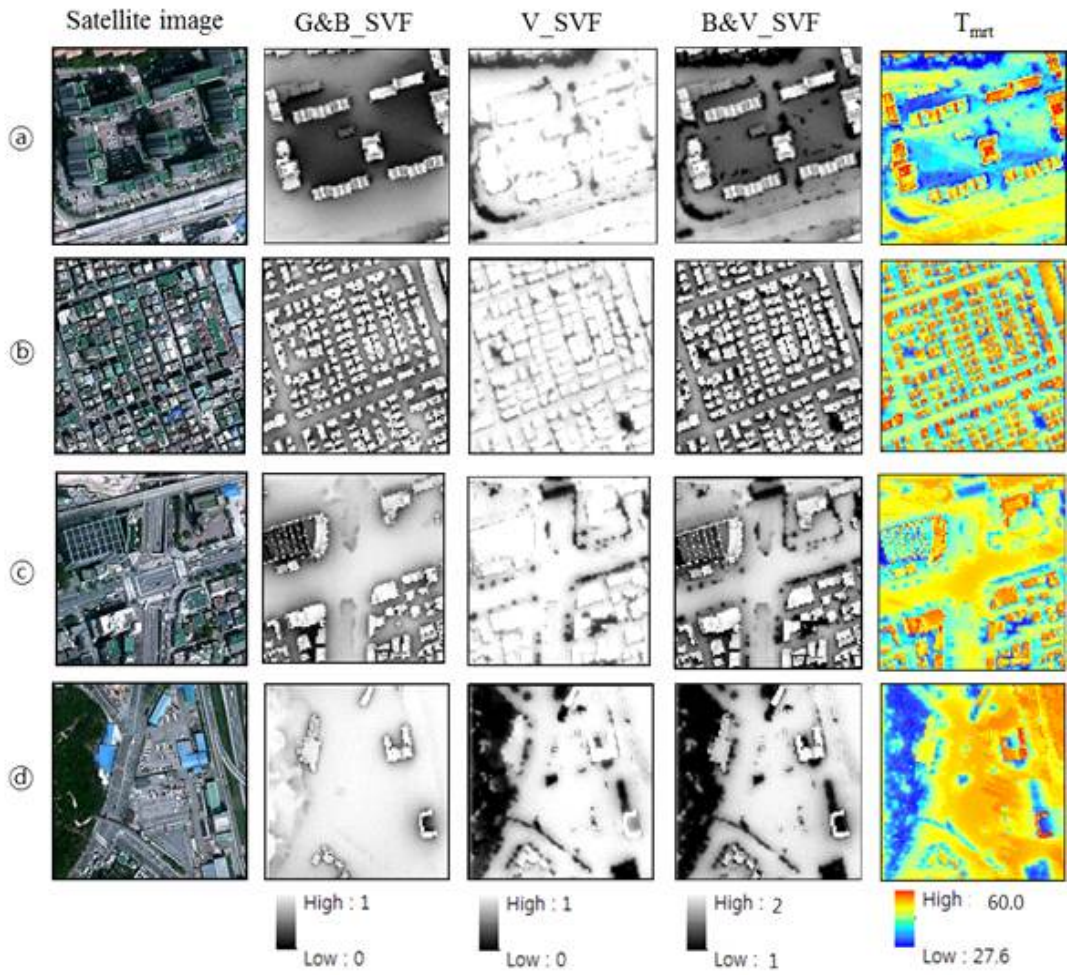

FIGURE 14. Satellite images of four urban settings showing the ground and buildings (G&B) sky view factor (SVF), vegetation (V) SVF, building and vegetation (B&V) SVF, and T_{mrt} (mean radiant temperature).

detailed thermal vulnerability assessment using the SOLWEIG model.

4. Mean radiant temperature variation in different urban settings

To analyse the difference in radiation at the pedestrian level within the 4 km^2 study area, four urban building settings were classified according to the characteristics of the surrounding structures (Fig. 12). Setting 'a' was an open high-rise apartment residential area, 'b' was a compact low-rise residential area representing multi-family housing, 'c' was a point where two major roads crossed, and 'd' was a vegetated area where pedestrians were assumed to

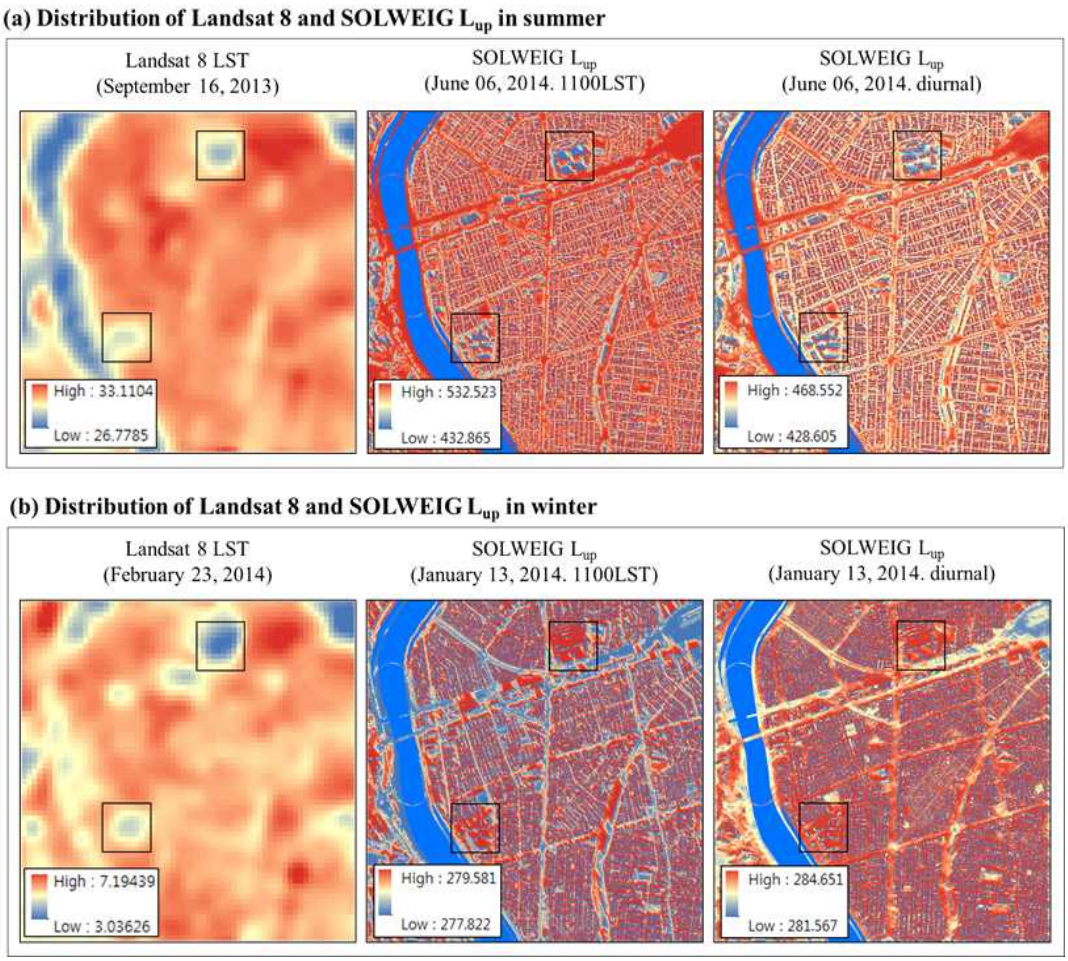

FIGURE 15. Comparison of satellite image surface temperatures from Landsat 8 and SOLWEIG simulation results.

be located between trees. The mean radiation temperature (T_{mrt}) calculated from the radiation fluxes is the temperature at which the solar radiation at the pedestrian's standing position can be influenced by considering the shielding effect of the surrounding structure; i.e., the degree to which the thermal effect is added or subtracted by the urban structure.

Each site was computed using the time it directly received the effect of solar radiation. Site 'a' included 5 h (09:00 to 14:00 LST) and site 'b' included 9 h (08:00 to 17:00 LST). Site 'b' had a longer time period owing to lower building height, but site a' had reduced SVF, resulting in a higher shadow effect and consequently lower T_{mrt}. Site 'c' had a high SVF value with almost no influence from buildings or vegetation. On the road, the solar

radiation time was at its maximum; therefore, T_{mrt} was consistently high. For site 'd', the building SVF was as high as 0.943, but the vegetation SVF was 0.113, with some places 88.7% of the area in the shadow of trees, resulting in the lowest T_{mrt} (Fig. 13).

Through this model, heat input, absorption, and emission relationships can be analysed according to the type of buildings (and vegetation) and canopy (Fig. 14). Given the sky is covered by either the terrain and buildings, vegetation, or buildings and vegetation, the blocking effect of solar radiation was determined. Moreover, it was possible to identify where the influence of solar radiation was high and investigate areas with high heat stress in summer by analysing the mean radiant temperature that can detect the amount of radiation at pedestrian height.

The T_{mrt} at the surface between open high-rise buildings (site 'a') was 35 ℃ lower than the T_{mrt} at the surface between compact low-rise buildings (site 'b'). This indicates that compact low-rise residential settings have a higher thermal vulnerability than the open high-rise apartments.

5. Comparison with land surface temperature (LST)

The simulated L_{up} flux distribution due to the characteristics of the residential area was compared with the surface temperature calculated using satellite imagery (Fig. 15). The original Landsat satellite was launched by the US Geological Survey (USGS) and National Aeronautics and Space Administration (NASA) on 23 July 1972, and Landsat 8 was launched on 13 February 2013. The surface temperature is calculated using the TIRS (Thermal Infrared Sensor) channel 10 or 11, resulting in a temperature distribution. We used Landsat 8 satellite imagery from the summer (16 September 2013) and winter (23 February 2014), with minimal cloud effect, and the same time period as SOLWEIG. To select the day with the smallest atmospheric impact, we chose a day with less than 30% cloud cover in the image.

Images are collected over Korea once every 16 days, and the Seoul area was observed between 10:30 LST and 11:10 LST. Figure 13 shows the L_{up} fluxes calculated using the SOLWEIG model and surface temperatures during summer and winter calculated from the satellite images. The L_{up} fluxes were compared at 11:00 LST, similar to the time when the satellite image was captured; the mean daily L_{up} fluxes were also compared. Within the 4 km^2 study area, there are primarily compact low-rise residential areas, two apartment complexes, and rivers. As the 2013a version of SOLWEIG does not consider the characteristics of heat capacity and heat release from land cover, the river was arbitrarily masked.

In the future, calculation of land cover characteristics will be required (Lindberg *et al.,* 2016). The surface temperature results for Landsat 8 and the L_{up} fluxes were in agreement,

showing characteristically lower temperatures at the two apartment complexes.

Conclusions

In this study, we used solar radiance modelling to determine the pedestrian level mean radiant temperature (T_{mrt}) based on high resolution spatial urban settings in typical residential areas of Seoul metropolitan area. Such modelling based information is reliable, easy to deliver, and provides scientifically or visually informative results. The SVF, shadow pattern, radiant fluxes, and T_{mrt} were analysed in the context of building type and vegetation using a high resolution (2 m) SOLWEIG model. Simulated radiant flux results were compared using net radiometer observations in compact low-rise residential areas; a slight difference was observed between model and observation results in winter.

Overall, on both clear and cloudy days in summer and winter, the RMSE and R^2 were approximately 25 Wm^{-2} and 0.9, respectively. The effect of shadows created a difference in the length of incident sunshine on building types. Compact low-rise residential areas had a longer period of sunshine (10 h), while open high-rise apartment areas had shorter sunshine periods (5 h). In low-rise residential areas, where the shadow effect was smaller, the daytime Lup flux intensity was high. For this reason, T_{mrt} was relatively high during the day, whereas open high-rise residential areas exhibited daytime T_{mrt} that was lower by 3-5 ℃ owing to low SVF. This result indicates that Seoul's compact low-rise residential buildings have higher thermal vulnerability than relatively open high-rise apartments. In addition, sophisticated solar models have linked changes in the distribution of local temperature to changes in the sensible heat distribution; micro climates develop owing to variations in radiation emissions (Yi *et al.,* 2016). However, to obtain more detailed information on thermal comfort, it is important to consider factors such as traffic volume and anthropogenic heat in addition to buildings and vegetation. Furthermore, the study area here covered only a small part of Seoul Metropolitan Area (SMA). Thus, a substantial amount of detailed urban setting input data and computational hardware/software resources will be required to cover the entire SMA in order to develop city-wide summer heat stress information and mitigation strategies.

All available natural and artificial urban setting information for Seoul should be integrated for better management. For example, urban summer heat island management should include multiple types of data, including high-rise building shape, tree canopy cover type for providing better shade, and renewable energy use for better urban air quality. Hence, urban settings could be better planned and multi-functional. There are many functions that natural and artificial urban settings can provide for urban infrastructure services, such as urban

heat island management, water storage, wind corridor control, renewable energy, and support for urban biological diversity or ecological services such as biotopes, all of which are related to urban micro climate management. KAGIS

REFERENCES

Akbari, H., M. Pomerantz and H. Taha. 2001. Cool surfaces and shade trees to reduce energy use and improve air quality in urban areas. Solar Energy 70(3):295-310.

An, S.M., B.S. Kim, H.Y. Lee, C.H. Kim, C. Yi, J.H. Eum and J.H. Woo. 2014. Three-dimensional point cloud-based sky view factor analysis in complex urban settings. International Journal of Climatology 34(8):2685-2701.

An, S.M., H.G. Son, K.S. Lee and C. Yi. 2016a. A study of the urban tree canopy mean radiant temperature mitigation estimation. Journal of the Korean Institute of Landscape Architecture 44(1):93-106. (안승만, 손학기, 이규석, 이채연. 2016a. 도시림의 여름철 평균복사온도 저감 추정 연구. 한국조경학회지 44(1):93-106.)

An, S.M., S.J. Kim and H.C. Lee. 2016b. A Study on the Urban Area Micro climate Management Direction. KRIHS. (안승만, 김승종, 이형찬. 2016b. 도시지역 미기후 관리방안 연구. 국토연구원)

ASHRAE. 2001. ASHRAE Fundamentals Handbook 2001 (SI Edition) American Society of Heating, Refrigerating, and Air Conditioning Engineers, ISBN: 1883413885.

Jaenicke, B., F. Meier, F. Lindberg, S. Schubert and D. Scherer. 2016. Towards a city-wide analysis of mean radiant temperature at high spatial resolution: An example from Berlin, Germany. Urban, 1151:15.

Kim, K.R., C. Yi, J.S. Lee, F. Meier, B. Jaenicke, U. Fehrenbach and D. Scherer. 2014. BioCAS: Biometeorological climate impact assessment system for building-scale impact assessment of heat-stress related mortality. Die Erde, 145:62.

Konarska, J., F. Lindberg, A. Larsson, S. Thorsson and B. Holmer. 2014. Transmissivity of solar radiation through crowns of single urban trees-application for outdoor thermal comfort modelling. Theoretical and Applied Climatology 117(3-4):363-376.

Kwon, T.H., M.S. Park, C. Yi and Y.J. Choi. 2014. Effects of different averaging operators on the urban turbulent fluxes. Atmosphere-Korea 24(2):197-206. (권태헌, 박문수, 이채연, 최영진. 2014. 평균 방법이 도시 난류 플럭스에 미치는 영향. 대기지 24(2):197-206.)

Lindberg, F. and C.S.B. Grimmond. 2011. The influence of vegetation and building morphology on shadow patterns and mean radiant temperature in urban areas: model development and evaluation. Theoretical and Applied Climatology 105: 311-323.

Lindberg, F., B. Holmer and S. Thorsson. 2008. SOLWEIG 1.0 - Modelling spatial variations of 3D radiant fluxes and mean radiant temperature in complex urban settings. International Journal of Biometeorology 52:697-713.

Lindberg, F., S. Onomura and C.S.B. Grimmond. 2016. Influence of ground surface

characteristics on the mean radiant temperature in urban areas. International Journal of Biometeorology 60(9):1439-1452.

Lindberg, F., C.S.B. Grimmond, A. Gabey, B. Huang, C. W. Kent, Theeuwes Sun, N.E., Jarvi, L., H.C. Ward, I. Capel-Timms and Chang, Y. 2018. Urban Multi-scale Environmental Predictor(UMEP): An integrated tool for city-based climate services. Environmental Modelling & Software 99:70-87.

Ministry of Environment. 2011. Statistics on land / natural environment.

Park, M.S., S.H. Park, J.H. Chae, M.H. Choi, Y. Song, M. Kang and J.W. Roh. 2017. High-resolution urban observation network for user-specific meteorological information service in the Seoul Metropolitan Area, South Korea. Atmospheric Measurement Techniques 10(4).

Ratti, C. and P. Richens. 1999. Urban texture analysis with image processing techniques. In Computers in Building. Springer, Boston, MA.

SOLWEIG(2013) A climate design tool, User manual for version 2013a. Urban Climate Group, Department of Earth Sciences, University of Gothenburg Sweden.

Stewart, I.D. and T.R. Oke. 2012. Local climate zones for urban temperature studies. Bulletin of the American Meteorological Society 93(12):1879-1900.

VDI. 1994. VDI 3789, Part 2: Environmental meteorology, interactions between atmosphere and surfaces; calculation of the short- and long wave radiation. Beuth, Berlin. pp. 52.

Wang, Z., C.B. Schaaf, A.H. Strahler, M.J. Chopping, M.O. Roman, Y. Shuai, C.E. Woodcock, D.Y. Hollinger and D.R. Fitzjarrald. 2014. Evaluation of MODIS albedo product(MCD43A) over grassland, agriculture and forest surface types during dormant and snow-covered periods. Remote Sensing of Environment 140:60-77.

Yi, C., S.M. An, K. Kim, H.G. Kwon and J.S. Min. 2016. Surface micro-climate analysis based on urban morphological characteristics: temperature deviation estimation and evaluation. Atmosphere-Korea 26(3):445-459. (이채연, 안승만, 김규랑, 권혁기, 민재식. 2016. 도시의 지표 형태학적 특성에 기반한 지면미기후 분석: 기온추정 및 평가. 대기지 26(3):445-459)

Yi, C., K.R. Kim, S.M. An, Y.J. Choi, A. Holtmann, B. Jaenicke, U. Fehrenbach and D. Scherer. 2016. Estimating spatial patterns of air temperature at building-resolving spatial resolution in Seoul, Korea. International Journal of Climatology 36(2):533-549.

Yi, C., Y. Shin and S.M. An. 2017. A study on a comparison of sky view factors and a correlation with air temperature in the city. Atmosphere-Korea 27(4):483-498. (이채연, 신이레, 안승만. 2017. 하늘시계지수 비교 및 도시기온 상관성 연구: 강남 선정릉지역을 중심으로. 대기지 27(4):483-498)

Yi, C., S.M. An, K.R. Kim, Y.J. Choi and D. Scherer. 2012. Improvement of air temperature analysis by precise spatial data on a local-scale: a case study of Eunpyeong New-town in Seoul. Journal of the Korean association of geographic information studies 15(1):144-158. (이

채연, 안승만, 김규랑, 최영진, Dieter Scherer. 2012. 상세 공간정보를 활용한 국지기온 분석 개선: 서울 은평구 뉴타운 사례로. 한국지리정보학회지 15(1):144-158). KAGIS